Investigations on the tensile deformation of pure Mg and Mg–15Gd alloy by in-situ X-ray synchrotron radiation and visco-plastic self-consistent modeling

Xu, Yuling; Huang, Yuanding; Wang, Yuye; Gan, Weiming; Wang, Shiwei; Maawad, Emad; Schell, Norbert; Hort, Norbert

Published in:
Journal of Magnesium and Alloys

DOI:
10.1016/j.jma.2021.06.011

Publication date:
2023

Document Version
Publisher's PDF, also known as Version of record

Available online at www.sciencedirect.com

ScienceDirect

Journal of Magnesium and Alloys 11 (2023) 607–613

www.elsevier.com/locate/jma

Full Length Article

Investigations on the tensile deformation of pure Mg and Mg–15Gd alloy by *in-situ* X-ray synchrotron radiation and visco-plastic self-consistent modeling

Yuling Xu[a,b,*], Yuanding Huang[b], Yuye Wang[c], Weiming Gan[b], Shiwei Wang[c], Emad Maawad[b], Norbert Schell[b], Norbert Hort[b]

[a] *Chongqing Academy of Science and Technology, Chongqing 401123, China*
[b] *Institute of Materials Research, Helmholtz-Zentrum Geesthacht, Geesthacht 21502, Germany*
[c] *Shanghai Spaceflight Precision Machinery Institute, Shanghai 201600, China*

Received 20 January 2021; received in revised form 15 May 2021; accepted 20 June 2021
Available online 23 July 2021

Abstract

In this study, the texture evolutions of two Mg materials during tension are explored. *In-situ* X-ray synchrotron and Visco-Plastic Self-Consistent (VPSC) modeling are employed to investigate the different deformation modes between pure Mg and Mg–15Gd (wt.%) alloy. These two materials with a strong extrusion texture show large different slip/twinning activity behaviors during tensile deformation. The basal ⟨a⟩ slip has the highest contribution to the initial stage of plastic deformation for pure Mg. During the subsequent plastic deformation, the prismatic slip is dominant due to the strong ED // ⟨100⟩ fiber texture. In contrast, the deformation behavior of Mg–15Gd alloy is more complex. Twinning and basal slip are dominant at the early stage of plastic deformation, but further deformation results in the increased activation of prismatic and pyramidal slips. In comparison to pure Mg, the ratios of the critical resolved shear stress (CRSS) between non-basal slip and basal slip of the Mg–15Gd alloy are much lower.

Keywords: Mg alloy; Texture; Mechanical behavior; In-situ investigation.

1. Introduction

Magnesium alloy is one of the lightest structure metallic materials and is widely used in the aerospace, automobile, and rail transport industries [1,2]. However, Mg alloy with a hexagonal close-parked (HCP) crystal structure makes the activation of slip systems insufficient at room temperature, which normally results in poor ductility and absolute strength [3-5]. Thus, deeply understanding the plastic deformation mechanisms of Mg alloys is necessary for the improvement of their mechanical properties. In Mg and its alloys, the common basal and prismatic slips only contribute to two independent slip systems, while the pyramids offer four or five independent modes [6,7]. Twinning has also proven to be a high contributor to the deformation mechanism of Mg alloys [8,9]. The basal slip is the softest one and is always the first to be activated. Therefore, the critical resolved shear stress (CRSS) of non-basal slips is significantly higher than that of basal slips at room temperature [10,11].

Many previous works have shown that the additions of rare earth elements (REs) as solid solutes can have a beneficial effect on the deformation mechanism of Mg alloys [12,13]. Stanford et al. used *in-situ* neutron diffraction to examine the strengthening effect of adding Y to Mg alloys. Mg–0.5%Y and Mg–2.2%Y alloys showed a similar CRSS for basal slip and {102} twinning. The alloy with 2.2%Y

* Corresponding author at: Chongqing Academy of Science and Technology, Yangliu Road No.1, Chongqing 401123, China.
E-mail address: sharlin_xu@hotmail.com (Y. Xu).

https://doi.org/10.1016/j.jma.2021.06.011

showed a greater CRSS for $\langle \boldsymbol{c} + \boldsymbol{a} \rangle$ slip [14]. Maldar et al. used visco-plastic self-consistent (VPSC) modeling to simulate the tensile deformation of Mg–Nd alloy. It was found the Nd reduced the CRSS $_{prism}$ /CRSS $_{basal}$ ratio which enhanced the ductility [15]. Janhedi et al. reported that solute REs can largely harden the twinning resistance of Mg alloy [16]. S. Lee et al. found that {101} twins and {101}-{102} twins were not formed in Mg–1Gd alloy; instead, a small amount of {102} twins appear at the early stage of deformation, which is beneficial for the improvement of elongation [17].

Synchrotron radiation, or hard X-rays, have been proven to be a powerful method for analyzing microstructures and properties due to its high detectivity, strong transmissive ability, and large beam size [18]. Unlike regular analytical methods, e.g., X-ray diffraction (XRD) and electron back-scattered diffraction (EBSD), synchrotron radiation makes it possible to get the pole figures in a relatively short time and to detect a high number of grains while the alloy is undergoing constant loading. Valuable information, such as texture evolution, lattice strain evolution, elastic and plastic properties of crystallographic planes, and internal stress, can be obtained with synchrotron radiation test data [19]. The VPSC model is an efficient tool which is used to simulate the deformation modes and reveal the texture evolution of materials [20].

Among all REs, the element Gd exhibits some of the highest solid strengthening in Mg. Previous study shows that the prismatic slip was easily activated in an Mg–15Gd alloy under compressive deformation [21]. In this study, the texture evolution of pure Mg and Mg–15Gd alloy during tensile tests was investigated by employing the *in-situ* synchrotron X-ray diffraction. The CRSS and deformation mechanism of an Mg alloy with high Gd solid solutes were simulated using a VPSC framework to acquire a deeper understanding.

2. Experimental and data evaluation

The details of the material processes were published in a previous publication [22]. The average grain sizes of pure Mg and Mg–15Gd (wt.%) were 55 and 30 μm, respectively. A cylindrical tensile specimen with a 6 mm diameter, a 30 mm length, and threaded heads was machined along the extrusion direction of the extruded bars.

The measurements of the *in-situ* texture were performed at the Helmholtz-Zentrum Geesthacht GEMS outstation (P07) at Petra III (DESY, Hamburg). For this measurement, a high-energy X-ray beam with an energy of 87 keV and a beam size of 0.7 × 0.7 mm^2 was selected. The distance between the sample and detector was set at 1069 mm and was refined using LaB6 calibration powder. A universal test machine (UTM) with a capability of 20 kN was used to stretch the cylindrical specimens. *In-situ* tensile measurements were performed with the crosshead at 0.0166 mm/s at room temperature up to the ultimate tensile strength (UTS) [23]. The six specific strains for measuring the texture are listed in Table 1. At each measurement point of the pole figure, the loading machine was set to be in position control. The ω rotation angle for the incomplete pole figure measurements was from −65° to 65° with incremental steps of 5° For the acquisition of Debye–Scherrer rings at each ω angle, a flat panel Perkin Elmer XRD 1621 detector and a fast readout area detector with a 2048 × 2048 pixel matrix and a 200×200 μm^2 pixel size were used. The measurement of each incomplete pole figure took approximately 5 min. The tensile deformation rate chosen for the study was 1 × 10^{-3} s^{-1}. The measured incomplete pole figures were first calculated using an in-house program called SteCa. The data obtained from the measured incomplete pole figures were then used to generate complete pole figures by using the software toolbox MTEX in MATLAB [24]. Fig. 1 shows the partial caked images collected at

Table 1
Stress and strain values at the points of texture measurement.

Test point	Mg		Mg–15Gd	
	Strain [%]	Stress [MPa]	Strain [%]	Stress [MPa]
P1	0	0	0	0
P2	0.52	43	0.54	79
P3	0.96	82	1.03	147
P4	1.74	124	1.39	191
P5	3.33	159	2.22	240
P6	10.88	–	11.57	–

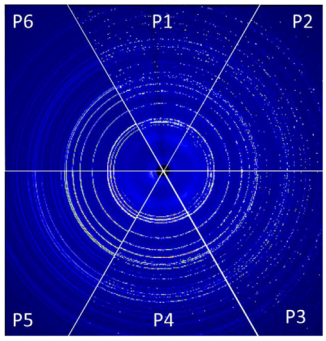

Fig. 1. The caked *in-situ* diffraction images of Mg–15Gd alloy collected at various tensile strain points. The tensile strain increases from the point "P1" to "P6". P1 to P4 were prior to yield point. The P5 and P6 were at quasi-steady state plastic deformation and after fracture, respectively.

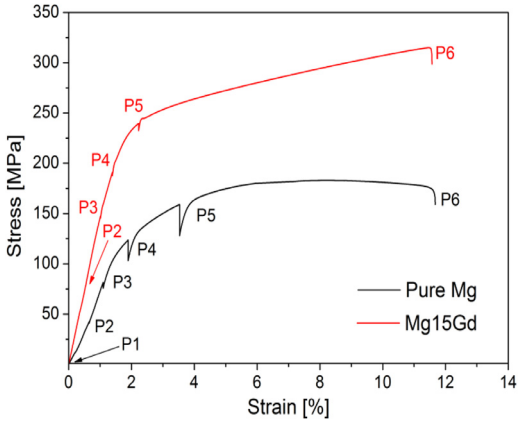

Fig. 2. Tensile curves of pure Mg and Mg–15Gd alloy.

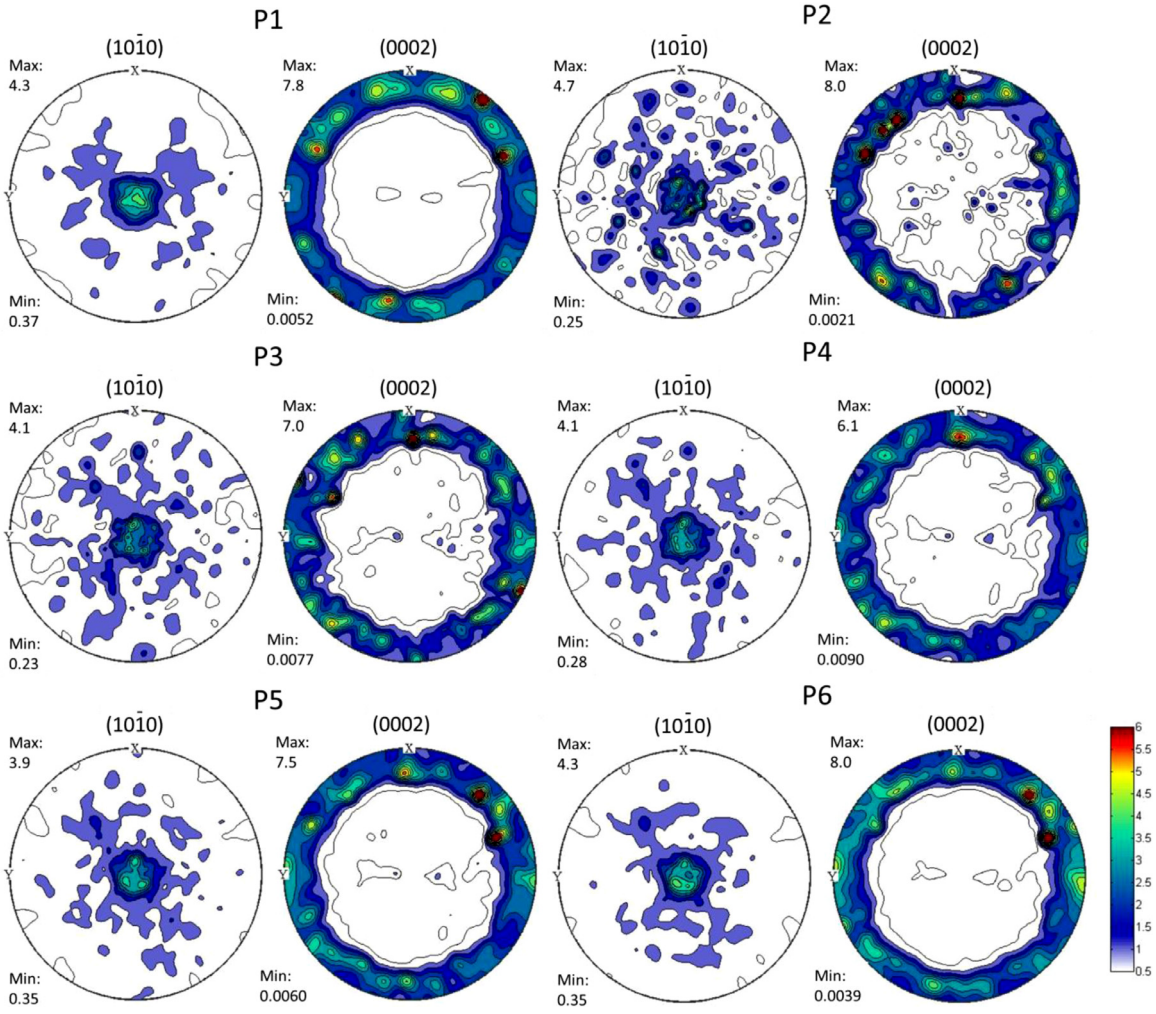

Fig. 3. Experimental {100} and (0002) pole figures from P1 to P6 for the tensile deformed pure Mg. LD is in the pole figure center.

these 6 measured points of Mg–15Gd alloy. The evolution of Debye-Scherrer rings can be observed clearly.

3. Modeling approach

The code package VPSC which was first developed by C.N. Tomé et al. was used to simulate and reflect the plastic behavior of polycrystalline pure Mg and Mg–15Gd alloy [20,25] . The interaction between each grain is explained by VPSC, which used Voce law to describe the hardening behavior of each slip system or twinning. The CRSS is given by:

$$\tau(\Gamma) = \tau_0 + (\tau_1 + \theta_1\Gamma)\left[1 - \exp(-\theta_0\Gamma/\tau_1)\right]$$

where τ_0, θ_0, θ_1, $(\tau_0+\tau_1)$ are the initial CRSS, the initial hardening rate, the asymptotic hardening rate and the back-extrapolated CRSS, respectively.

In the present work, four deformation systems, basal, prismatic ⟨a⟩, pyramidal II ⟨c + a⟩ slip and tensile twinning, were taken into considerations. For VPSC simulation, the *in-situ* measured initial texture pole figures were used as input data, and the Affine linearization scheme was selected to reflect the relationship between the stress and strain-rate. The τ_0, θ_0, τ_1 and θ_1 corresponding to each deformation system were obtained with simulated strain-stress and pole figures [26].

4. Results and discussion

4.1. In-situ tensile curves and texture

The *in-situ* tensile stress–strain curves of pure Mg and the Mg–15Gd alloy are shown in Fig. 2. The Mg–15Gd alloy has a higher yield strength and ultimate strength than pure Mg with values of 220 and 315 MPa, respectively. Those two samples have similar elongation with a value of about 11%. Table 1 lists the strain and stress values for the *in-situ* pole figures which are denoted by P1 to P6 for each sample. The measurement points from P1 to P4 are prior to the yield point, while the P5 and P6 are at quasi-steady state of plastic deformation and after fracture, respectively. Previous study results showed that the ductilizing of Mg–Gd alloys could be improved with moderate Gd in solid solutes. However, an increase in the Gd concentration results in a

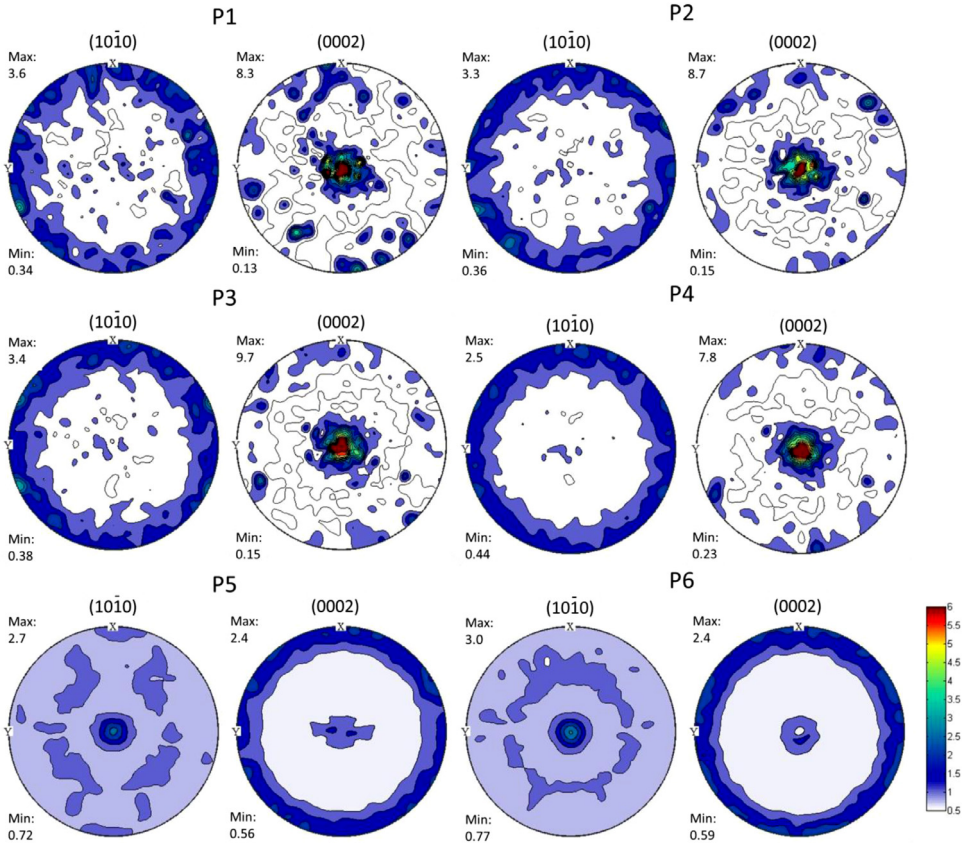

Fig. 4. Experimental of {100} and (0002) pole figures from P1 to P6 for the tensile deformed Mg–15Gd alloy. LD is in the pole figure center.

decrease in the elongation of Mg binary alloys. This phenomenon is found in both cast and wrought alloys [27,28]. Huang et al. showed that when increasing the Al concentration in an Mg–Mn alloy, the ductility initially increases, and a weaker ductility is obtained with higher Al concentrations [29].

The texture evolutions of pure Mg and the Mg–15Gd alloy during tensile deformation are presented in Figs. 3 and 4, respectively. About 30,000 and 160,000 grains contribute to the texture data for pure Mg and the Mg–15Gd alloy, respectively. The tensile direction is located at the center of the pole figure. Both specimens exhibited a strong texture in the as-extruded state (P1). From the pole figures, the basal planes of most grains in Mg are approximately parallel to the ED, which indicates a typical ED//{0001} basal fiber texture.

In contrast, the grain orientation distribution of the Mg–15Gd alloy is different, as the basal plane is essentially perpendicular to the loading direction, i.e., ED⊥{0001} basal fiber. From points P1 to P4, i.e., at the elastic stage (before yielding), the grains retain their initial orientations. When the tensile strain is further increased to P5, the texture distribution is significantly changed under a stress of 240 MPa. The reorientation occurs in most grains and leads to a distribution that results in the basal planes becoming parallel to the tensile direction. The maximum intensity of the {0002} pole figure is decreased to 2.4 mrd at point P5.

4.2. Simulation results with the VPSC model

The parameters relative to Voce model used in VPSC are shown in Table 2 and include τ_0, τ_1, θ_0, and θ_1. The VPSC modeling confirmed that the initial CRSS for all studied deformations of Mg–15Gd are much higher than that for pure Mg. The part of Gd with a solid solution in Mg increases the $CRSS_{basal}$ from 5 MPa to 60 MPa. The simulated strain-stress curves and predicted active deformation modes of the materials are illustrated in Fig. 5. The simulated curves are in particularly good agreement with the data from the experiments. At the beginning of tensile deformation, the deformation is mainly proceeded by the basal slip in pure Mg. With the deformation continuing, the prismatic slip $\langle \mathbf{a} \rangle$ is activated and its slip start to accommodate the deformation. During the whole tensile deformation, the tensile twinning and pyramidal slip $\langle \boldsymbol{c} + \boldsymbol{a} \rangle$ contribute much less to the deformation. Unlike in pure Mg, the Mg–15Gd alloy exhibit a different deformation mode. At the early stage of deformation, both the basal slip and tensile twinning dominate the deformation, which explains the sudden change in the grain orientation from P4 to P5. When the deformation strain in-

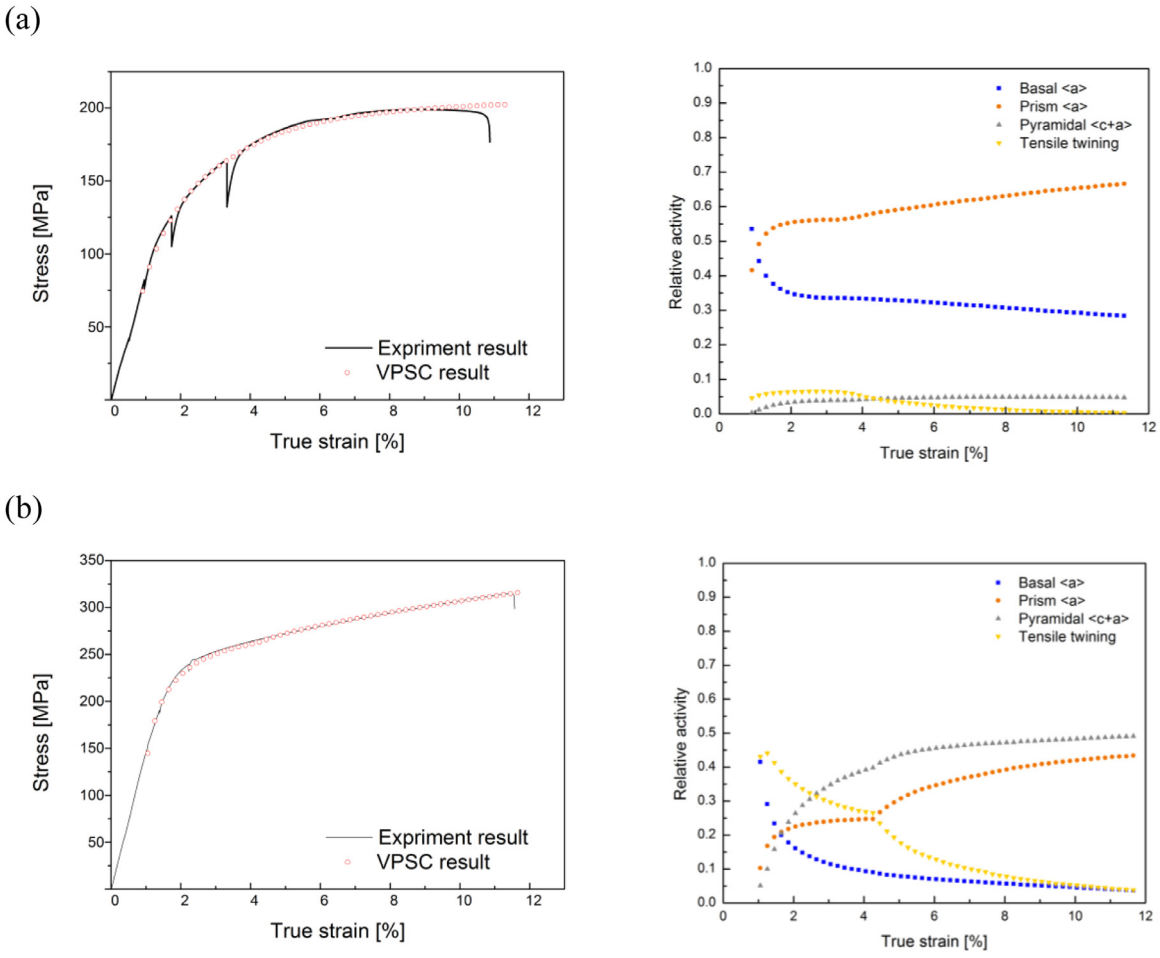

Fig. 5. Simulated stress-strain curves and predicted deformation modes for (a) pure Mg and (b) Mg–15Gd alloy.

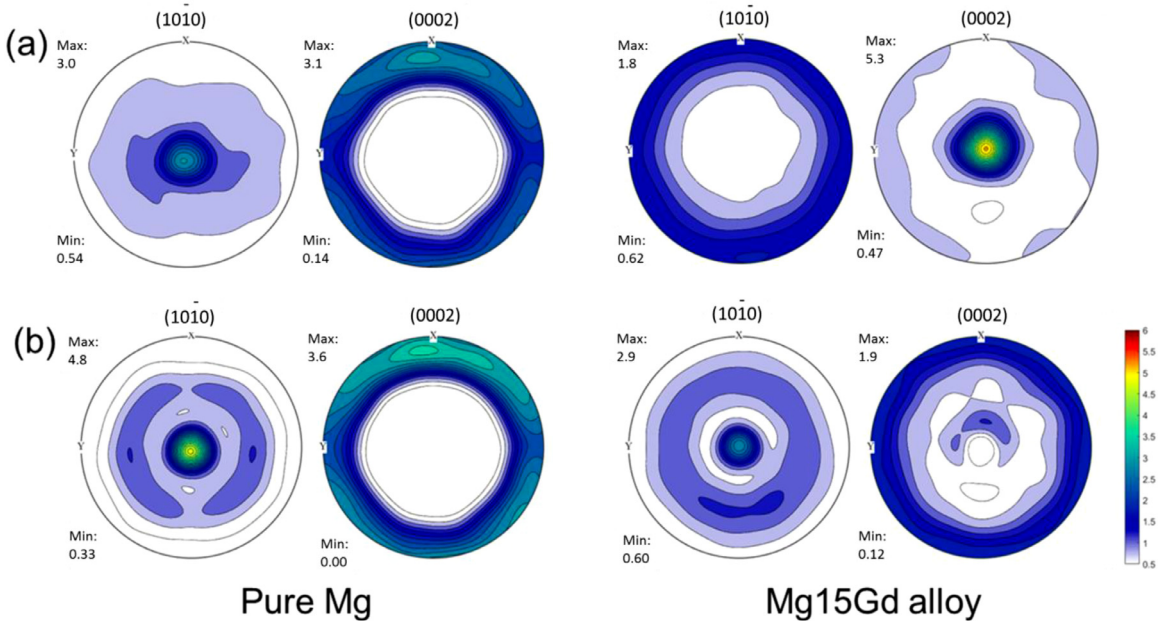

Fig. 6. Simulated pole figures at (a) initial point (P1) and (b) after fracture (P6) for pure Mg and Mg–15Gd alloy.

Table 2
Simulation parameters used in VPSC for pure Mg and Mg–15Gd alloy.

Deformation mode		Pure Mg				Mg–15Gd			
		τ_0 [MPa]	τ_1 [MPa]	θ_0	θ_1	τ_0 [MPa]	τ_1 [MPa]	θ_0	θ_1
Basal <***a***>	{0002}<110>	5	30	1100	0	60	90	4500	500
Prism <***a***>	{100}<110>	50	63	1400	0	125	30	100	80
Pyramidal II <***c*** + ***a***>	{112}<113>	75	90	2500	0	130	10	600	70
Tensile twinning	{102}<101>	30	0	30	30	70	50	2000	80

creases to 2%, the contribution to deformation from prismatic slip ⟨**a**⟩ and pyramidal slip ⟨***c*** + ***a***⟩ could not be neglected, and both slips play a key role in the subsequent stage of deformation.

The texture evolution and deformation modes of Mg and Mg–15Gd alloys during compression tests have been discussed in previous study [21]. The c/a ratio of Mg cell decreases to 1.617 with addition of Gd, leading to the different deformation modes. In addition, the solute/dislocation interaction energy and stacking fault energy are also consideration factors [30-32]. According to the VPSC simulation results, the initial CRSSs of different slip systems and tensile twinning of Mg–15Gd alloy are higher than that of pure Mg. This is the main reason for its greater yield strength and ultimate tensile strength. Compared to other alloying elements such as Y [14], Al [33], Nd, and Ca [15], the part of Gd with solid solution in Mg has a much higher effect on the $CRSS_{basal}$ of Mg. The possible reason is that high amount of Gd with solid solution alter the c/a ratio of Mg cell [34]. This could significantly enhance the bond energy between atoms [35]. However, in this case, the CRSS of the pyramidal slip and extension twinning are increased relatively lower rate than that of Mg–Gd–Y alloys [36].

Fig. 6 displays the simulated {100} and (0002) pole figures at the initial point (P1) (Fig. 6(a)) and after the fracture point (P5) (Fig. 6(b)) for pure Mg and Mg–15Gd alloy, respectively. The simulated pole figures generally match those of the *in-situ* measurements. Based on the simulated pole figures, there is only a little change in the distribution of grain orientations for pure Mg because of the entire tensile deformation. During deformation, both the basal and prismatic slip dominated, and the pyramidal slip increase by a minimal amount. In contrast, if comparing at the initial deformation to the final stage of deformation, the grain orientations of Mg–15Gd alloy are changed significantly. The texture changes from the basal to prismatic slip. Based on the activation of deformation modes in the Mg–15Gd alloy, the change in grain orientation can mainly be attributed to the coordination of tensile twinning and the pyramidal slip during the later stage of deformation.

Finally, the CRSS ratios of the prismatic and pyramidal planes to the basal plane are calculated as $CRSS_{prism}/CRSS_{basal}=10$ and $CRSS_{pyramidal}/CRSS_{basal}=15$ for pure Mg with Mg–15Gd alloys, these two ratios reduce to 2.08 and 2.17, respectively, which indicates that the non-basal slip in an Mg–15Gd alloy is initiated more easily. Indeed, the CRSS ratios of Mg–15Gd alloys are much lower than that of non-RE Mg alloys, such as AZ31 [37], Mg–Ca [15] and ZK60 alloys [38]. It can be ratiocinated that the addition of Gd in Mg is not only beneficial for the improvement of its strength but also for its deformation homogeneity owing to the promoted non-basal slip.

5. Conclusions

The tensile deformation of extruded pure Mg and an Mg–15Gd alloy is investigated by using *in-situ* synchrotron radiation. It was further explored and discussed by VPSC modeling. The following conclusions can be drawn:

(1) The es-extruded Mg and the Mg–15Gd alloy show a similar elongation, but the Mg–15Gd alloy double the yield and ultimate stress of pure Mg. The VPSC model successfully simulates the macroscopic stress-strain curves and texture evolutions for these two alloys.
(2) Both the basal and prismatic ⟨**a**⟩ slip dominate the whole deformation in pure Mg. In contrast, in the Mg–15Gd alloy both the basal slip and tensile twinning play a key role in the initial deformation. With the deformation continuing, they are weakened and replaced by the prismatic ⟨**a**⟩ and pyramidal ⟨***c*** + ***a***⟩ slip, especially at the later stage of deformation. The different deformation modes of Mg and the Mg–15Gd alloy results in their different texture evolution.
(3) The Mg–15Gd alloy has a much higher CRSS for basal, ⟨***c*** + ***a***⟩ slip and {102} twinning than pure Mg dose. The addition of Gd in Mg remarkably reduces the $CRSS_{prism}/CRSS_{basal}$ and $CRSS_{pyramidal}/CRSS_{basal}$ ratio.

Acknowledgments

The authors acknowledge the help and support of Mr. Günther Meister (MagIC, HZG) during casting. The authors thank Prof. Walter Reimers (FMW, TU Berlin) for offering help of extrusion processing. The present work was sponsored by the China Postdoctoral Science Foundation (Grant No. 2020M673156) and Shanghai Pujiang Program (Grant No. 20PJ1404900). We acknowledge DESY (Hamburg, Germany), a member of the Helmholtz Association HGF, for the

provision of experimental facilities. Parts of this research were carried out at P07 beamline of HZG.

References

[1] T.B. Abbott, Corrosion 71 (2) (2014) 120–127.
[2] S. You, Y. Huang, K.U. Kainer, N. Hort, J. Magnes. Alloys 5 (3) (2017) 239–253.
[3] Z.-Z. Shi, Y. Zhang, F. Wagner, P.-A. Juan, S. Berbenni, L. Capolungo, J.-S. Lecomte, T. Richeton, Acta Mater. 83 (2015) 17–28.
[4] M.R. Barnett, Mater. Sci. Eng.: A 464 (1–2) (2007) 1–7.
[5] M.R. Barnett, Mater. Sci. Eng.: A 464 (1–2) (2007) 8–16.
[6] M.H. Yoo, Metall. Trans. A 12 (1981) 409–418.
[7] C. Cáceres, P. Lukáč, Philos. Mag. 88 (7) (2008) 977–989.
[8] R.K. Mishra, A. Brahme, R.K. Sabat, L. Jin, K. Inal, Int. J. Plast. 117 (2019) 157–172.
[9] B. Song, Q. Yang, T. Zhou, L. Chai, N. Guo, T. Liu, S. Guo, R. Xin, J. Mater. Sci. Technol. 35 (10) (2019) 2269–2282.
[10] L. Jiang, J.J. Jonas, R.K. Mishra, A.A. Luo, A.K. Sachdev, S. Godet, Acta Mater. 55 (11) (2007) 3899–3910.
[11] J. Koike, T. Kobayashi, T. Mukai, H. Watanabe, M. Suzuki, K. Maruyama, K. Higashi, Acta Mater. 51 (7) (2003) 2055–2065.
[12] J. Bohlen, S. Yi, D. Letzig, K.U. Kainer, Mater. Sci. Eng.: A 527 (26) (2010) 7092–7098.
[13] Y. Lu, Q. Wang, X. Zeng, W. Ding, C. Zhai, Y. Zhu, Mater. Sci. Eng. A 278 (2000) 11.
[14] N. Stanford, R. Cottam, B. Davis, J. Robson, Acta Mater. 78 (2014) 1–13.
[15] A. Maldar, L. Wang, G. Zhu, X. Zeng, J. Magnes. Alloys 8 (1) (2020) 210–218.
[16] M. Jahedi, B.A. McWilliams, P. Moy, M. Knezevic, Acta Mater. 131 (2017) 221–232.
[17] S.W. Lee, S.-H. Kim, W.-K. Jo, W.-H. Hong, W. Kim, B.G. Moon, S.H. Park, J. Alloys Compd. 791 (2019) 700–710.
[18] H.-G. Brokmeier, Hard X-rays for in situ strain and texture measurements, 26(3) (2009) 117–124.
[19] Z.Y. Zhong, H.G. Brokmeier, E. Maawad, N. Schell, Mater. Sci. Eng.: A 639 (2015) 519–525.
[20] R.A. Lebensohn, C.N. Tomé, P.J. Maudlin, J. Mech. Phys. Solids 52 (2) (2004) 249–278.
[21] Y. Xu, Y. Huang, Z. Zhong, S. You, W. Gan, B. Xiao, E. Maawad, N. Schell, F. Gensch, F. Pan, N. Hort, Mater. Sci. Eng.: A 774 (2020).
[22] Y. Xu, F. Gensch, Z. Ren, K.U. Kainer, N. Hort, Progr. Nat. Sci.: Mater. Int. 28 (6) (2018) 724–730.
[23] Z.Y. Zhong, H.G. Brokmeier, W.M. Gan, E. Maawad, B. Schwebke, N. Schell, Mater. Charact. 108 (2015) 124–131.
[24] G. Nolze, R. Hielscher, J. Appl. Crystallogr. 49 (5) (2016) 1786–1802.
[25] R.A. Lebensohn, C.N. Tomé, Mater. Sci. Eng.: A 175 (1) (1994) 71–82.
[26] R.A. Lebensohn, C.N. Tome, Manual for Code, Visco-Plastic Self-Consistent (VPSC), Los Alamos National Laboratory, 2017.
[27] Y. Xu, Investigations on Young's Modulus and Strengthening Mechanisms of Mg-Gd and Mg-Nd Alloys, Technische Universität Berlin, 2018.
[28] Y. Huang, Y. Xu, S. You, W. Gan, K.U. Karl, N.J.M.W.C. Hort, Strengthening and ductilizing of magnesium alloying with heavy rare earth elements, MATEC Web Conf. 188 (2018) 03021.
[29] X. Huang, K. Suzuki, Y. Chino, M. Mabuchi, Mater. Sci. Eng.: A 633 (2015) 144–153.
[30] J.A. Yasi, L.G. Hector, D.R. Trinkle, Acta Mater. 60 (5) (2012) 2350–2358.
[31] A. Tehranchi, B. Yin, W.A. Curtin, Acta Mater. 151 (2018) 56–66.
[32] Z. Pei, R. Li, J.-F. Nie, J.R. Morris, Mater. Des. 165 (2019) 107574.
[33] J.J. Bhattacharyya, S.R. Kada, M.R. Barnett, S.R. Agnew, Materialia 6 (2019) 100308.
[34] M. Yoo, S. Agnew, J. Morris, K. Ho, Mater. Sci. Eng.: A 319 (2001) 87–92.
[35] L. Gao, J. Zhou, Z. Sun, R. Chen, E. Han, Chin. Sci. Bull. 56 (10) (2011) 1038.
[36] J. Sun, L. Jin, S. Dong, J. Dong, Z. Zhang, F. Wang, W. Ding, A.A. Luo, Mater. Des. 122 (2017) 164–171.
[37] B. Raeisinia, S.R. Agnew, A. Akhtar, Metall. Mater. Trans. A 42 (5) (2010) 1418–1430.
[38] W. Ren, R. Xin, J. Xu, B. Song, L. Zhang, Q. Liu, J. Alloys Compd. 792 (2019) 610–616.